



merger fraction increases significantly (López-Sanjuan et al. 2010; Bluck et al. 2012; Ownsworth et al. 2014). Tentative measurements of the merger fractions at redshifts as high as  $4 \leq z \leq 6$  were first presented in Conselice & Arnold (2009), making use both pair-count and morphological estimates merger estimates. For both estimates, the fraction of galaxies in mergers declines past  $z \sim 4$ , supporting the potential peak in the galaxy merger fraction at  $1 \lesssim z \lesssim 2$  reported by Conselice et al. (2008; morphology) and Ryan et al. (2008; close-pairs). However, as this study was limited to only optical photometry in the very small but deep Ultra Deep Field (Beckwith et al. 2006), the results were subject to small sample sizes and a lack of robust photometric redshift and stellar mass estimates.

When studying galaxy close-pair statistics, to satisfy the close pair criterion two galaxies must firstly be within some chosen radius (typically 20 to 50 kpc) in the plane of the sky and secondly within some small velocity offset along the redshift axis. The typical velocity offset required is  $\Delta 500 \text{ km s}^{-1}$ , corresponding to a redshift offset of  $\Delta z \leq$ . However, this clearly leads to difficulties when studying the close-pair statistics of deep photometry surveys, the scatter on even the best photometric redshift estimates is  $\sigma_z \geq$ . Moreover, measuring systemic spectroscopic redshifts is increasingly difficult at high-redshift due to the increased difficulty in observing multiple emission lines for systemic redshift estimates (Stark et al. 2014). The required redshift accuracy is often beyond spectroscopy even if such data was available for all galaxies in a survey.

To estimate the merger fractions of galaxies in wide-area photometric redshift surveys or at high-redshift, we must find a methodology which allows us to overcome the limitations of redshift accuracy in these surveys and correct or account for the pairs observed in the plane of the sky which are due to chance alignments along the line-of-sight. Various approaches have been used to overcome this limitation, including the use of de-projected two-point correlation functions (Bell et al. 2006), correcting for chance pairs by searching over random positions in the sky (Kartaltepe et al. 2007), and integrating the mass or luminosity function around the target galaxy to estimate the number expected number of random companions (Le Fèvre et al. 2000; Bluck et al. 2009; Bundy et al. 2009).

In López-Sanjuan et al. (2015), a new method for estimating reliable merger fractions through the photometric redshift probability distribution functions (PDFs) of galaxies. In this paper we apply this PDF close-pair technique presented in López-Sanjuan et al. (2015) to the deep CANDELS (Grogin et al. 2011; Koekemoer et al. 2011) photometric survey in order to estimate the major merger rate of massive galaxies at  $z \geq 2$ . In addition to the the greatly improved number statistics available due to increased volume probed by the CANDELS survey (compared to the Hubble UDF alone), this study also benefits from the use of deep *Spitzer* IRAC observations for improved photometric redshift and stellar mass estimation at high-redshift. It has been shown that sampling galaxies SEDs above the Lyman

break is essential for reliably selecting galaxies at  $z > 5$  (McLure et al. 2011) and estimating reliable photometric redshifts and stellar masses.

Throughout this paper all quoted magnitudes are in the AB system (Oke & Gunn 1983) and we assume a  $\Lambda$ -CDM cosmology ( $H_0 = 70 \text{ km s}^{-1} \text{ Mpc}^{-1}$ ,  $\Omega_m = 0.3$  and  $\Omega_\Lambda = 0.7$ ) throughout. Quoted observables are expressed as actual values assuming this cosmology unless explicitly stated otherwise. Note that luminosities and luminosity based properties such as observed stellar masses scale as  $h^{-2}$ .

## 2 DATA

In this work we make use of the CANDELS multi-wavelength photometry catalog in the GOODS South field. Details of the catalog, the space and ground-based imaging and its reduction can be found in Duncan et al. (2014) and Guo et al. (2013) and references therein.

## 3 METHODOLOGY

The primary goal of analysing the statistics of close pairs of galaxies is to estimate the fraction of galaxies which are in the process of merging. From numerical simulations (Kitzbichler & White 2008), it is well understood that the vast majority of galaxies within some given physical separation will eventually merge. For spectroscopic studies in the nearby Universe, a close pair is often defined by a projected separation,  $r_p$ , in the plane of the sky of  $r_p < 20$  to  $50 \text{ h}^{-1} \text{ kpc}$  and a separation in redshift or velocity space of  $\Delta v \leq 500 \text{ km s}^{-1}$ .

Armed with a measure of the statistics of galaxies which satisfy these criteria within a sample, we can then estimate the corresponding merger fraction,  $f_m$ , defined as

$$f_m = \frac{N_{\text{pairs}}}{N_T}, \quad (1)$$

where  $N_{\text{pairs}}$  and  $N_T$  are the number of galaxy pairs and the total number of galaxies respectively within some target sample, e.g. a volume limited sample of mass selected galaxies.

In this work, we analyse the galaxy close-pairs through the use of their photometric redshift probability density functions (PDFs). The use of photometric redshift PDF takes into account the uncertainty in galaxy redshifts in the pair selection and the effect of the redshift uncertainty on the projected distance and derived galaxy properties. In the following section we outline the method as applied in this work and how it differs to that presented in López-Sanjuan et al. (2015) in the use of stellar mass instead of luminosity when defining the close-pair selection criteria as well as our use of flux-limited samples and the corresponding corrections.

### 3.1 Selecting initial potential close-pairs

Before defining a target-sample, we first clean the photometric catalog for sources which have a high likelihood of being stars or image artefacts. Stars are defined as sources which have a high SExtractor stellarity parameter ( $> 0.95$ ) and/or have an SED which is consistent with being a star (as determined in the CANDELS official photometric redshift release, Dahlen et al. (2013)). Sources which are flagged as artefacts or strongly affected by bright stars in the field (and their diffraction spikes) as determined by the photometry flag map (Guo et al. 2013) are also excluded.

Once an initial sample has been selected (see Section 3.3), we use *kd* trees based on the target and full galaxy samples to efficiently search for projected close pairs (Maewongvatana & Mount 1999). We search for the initial close pairs within the maximum angular separation for the desired physical separation across the full redshift range of interest ( $z > 2$  in this work). Duplicates are then removed from the initial list of close-pairs (with the primary galaxy determined by the galaxy with the highest stellar mass at its corresponding best-fit photometric redshift) to create the list of galaxy pairs for PDF analysis. Because the PDF analysis makes use of all available information to determine the pair fractions, it is applied to all galaxies within the initial sample simultaneously, with the redshift and mass ranges of interest determined by the selection functions and integration limits outlined in the following sections.

### 3.2 The pair probability function

For a given projected close-pair of galaxies within the full galaxy sample, the combined redshift probability function,  $\mathcal{Z}(z)$ , is defined as

$$\mathcal{Z}(z) = \frac{2 \times P_1(z) \times P_2(z)}{P_1(z) + P_2(z)} = \frac{P_1(z) \times P_2(z)}{N(z)} \quad (2)$$

where  $P_1(z)$  and  $P_2(z)$  are the photometric redshift probability distribution functions (PDFs) for the primary and secondary galaxies in the projected pair. The normalisation,  $N(z) = (P_1(z) + P_2(z))/2$ , is implicitly constructed such that  $\int_0^\infty N(z) dz = 1$  and  $\mathcal{Z}(z)$  therefore represents the number of close pairs at redshift  $z$  for the projected close pairs being studied. The total number of pairs for a given system is then given by

$$\mathcal{N}_z = \int_0^\infty \mathcal{Z}(z) dz. \quad (3)$$

and can range between 0 and 1. As each initial target galaxy can have more than one close companion, each potential galaxy pair is analysed separately and included in the total pair count. We note that because the initial list of projected pairs is we cleaned for duplicates before analysing the redshift PDDs, if the two galaxies in a system (with redshift PDFs of  $P_1(z)$  and  $P_2(z)$ ) both satisfy the primary galaxy selection function, the number of pairs is not doubly counted.

As the redshift probability function takes into account

the line-of-sight information for the potential galaxy pair, two additional binary redshift masks are required to enforce the additional pair selection criteria. These masks are equal to one at a given redshift when the selection criteria are satisfied and zero otherwise. As above, we follow the notation outlined in López-Sanjuan et al. (2015) and define the angular separation mask,  $\mathcal{M}^\theta(z)$ , as

$$\mathcal{M}^\theta(z) = \begin{cases} 1, & \text{if } \theta_{min}(z) \leq \theta \leq \theta_{max}(z) \\ 0, & \text{otherwise,} \end{cases} \quad (4)$$

where the angular separation between the galaxies in a pair as a function of redshift is denoted  $\theta(z)$ . The angular separation is a function of the projected distance  $r_p$  and the angular diameter distance,  $d_A(z)$ , for a given redshift and cosmology, i.e.  $\theta_{max}(z) = r_p^{max}/d_A(z)$  and  $\theta_{min}(z) = r_p^{min}/d_A(z)$ .

The pair selection mask, denoted  $\mathcal{M}^{pair}(z)$ , is where our method differs to that outlined by López-Sanjuan et al. (2015). Rather than selecting galaxy pairs based on the luminosity ratio, we instead select based on the estimated stellar mass ratio. We define our pair-selection mask as

$$\mathcal{M}^{pair}(z) = \begin{cases} 1, & \text{if } M_{\star}^{lim,1}(z) \leq M_{\star,1}(z) \leq M_{\star,max} \\ & \text{and } M_{\star}^{lim,2}(z) \leq M_{\star,2}(z) \\ 0, & \text{otherwise.} \end{cases} \quad (5)$$

where  $M_{\star,1}(z)$  and  $M_{\star,2}(z)$  are the stellar mass as a function of redshift, details of how  $M_{\star}(z)$  is calculated for each galaxies are discussed in Section 3.4. The flux-limited mass cuts,  $M_{\star}^{lim,1}(z)$  and  $M_{\star}^{lim,2}(z)$ , are given by

$$M_{\star}^{lim,1}(z) = \max\{M_{\star}^{min}, M_{\star}^{flux}(z)\} \quad (6)$$

and

$$M_{\star}^{lim,2}(z) = \max\{\mu M_{\star}^1(z), M_{\star}^{flux}(z)\} \quad (7)$$

respectively, where  $M_{\star}^{flux}(z)$  is the redshift dependent mass completeness limit outlined in Section 3.5.1 and  $M_{\star}^{min}$  and  $M_{\star}^{max}$  are the lower and upper ranges of our target sample of interest. The mass ratio  $\mu$  is typically defined as  $\mu = 1/4$  for major mergers and  $\mu = 1/10$  for minor mergers, throughout this work we set  $\mu = 1/4$  by default unless otherwise stated. This pair selection mask ensures the following criteria are met at each redshift. Firstly, the primary galaxy is within the mass range of interest. Secondly, the mass ratio between the primary and secondary galaxy is within the desired range (e.g. for selecting major or minor mergers). And finally that both the primary and secondary galaxy are above the mass completeness limit at the corresponding redshift. We note that the first criteria of Equation 5 also constitutes the selection function for the primary sample, given by

$$S(z) = \begin{cases} 1, & \text{if } M_{\star}^{lim,1}(z) \leq M_{\star,1}(z) \leq M_{\star,max} \\ 0, & \text{otherwise.} \end{cases} \quad (8)$$

With these three properties in hand for each potential companion galaxy around our primary target, the pair-probability function, PPF( $z$ ), is then given by

$$PPF(z) = \mathcal{Z}(z) \times \mathcal{M}^\theta(z) \times \mathcal{M}^{pair}(z). \quad (9)$$

In Section 3.6 we outline how this pair-probability function is integrated to determine the photometric pair-probability, but first we outline how the photometric redshifts and stellar masses used in this analysis were estimated and then outline the steps taken to correct for selection effects within the data.

### 3.3 Photometric redshifts

Photometric redshifts for all sources are calculated using the EAZY photometric redshift code (Brammer et al. 2008). The redshifts were fit to all available photometric bands for each field as outlined in Section 2 and made use of the default EAZY reduced template set plus the addition of a young Ly $\alpha$  emitting galaxy template based on the spectrum of Erb et al. (2010). We construct the redshift probability distribution (PDF,  $P(z)$ ) for each galaxy from its  $\chi^2$  distribution following  $P(z) \propto \exp(-\chi_z^2/2)$ .

When calculating the galaxy PDFs we do not make use of a luminosity or colour dependent redshift prior as is commonly done (Brammer et al. 2008; Dahlen et al. 2013). This choice is largely motivated by the lack of simulated redshift distributions which are well constrained at high redshifts, existing semi-analytic models agree well with observations at  $z < 2$  but begin to diverge as redshift increases (Henriques et al. 2012).

Furthermore, the use of a prior which is only dependent on a galaxy's luminosity and not its colour or wider SED properties could significantly bias the estimation of close-pairs using redshift PDFs. Consider a pair of galaxies at identical redshifts and with stellar population properties, the only difference is the stellar mass of the galaxy. A luminosity dependent prior will change the posterior probability distribution for each galaxy individually and could erroneously decrease the integrated pair probability. The effects of luminosity based priors on redshift PDFs at  $z < 3$  where SAMs are much better constrained are explored in further detail in Mundy et al. in prep.

As discussed in Hildebrandt et al. (2008) and Dahlen et al. (2013), the redshift probability density functions output by photometric redshift codes can often be an inaccurate representation of the true photometric redshift error. This inaccuracy can be due to under- or over-estimates of photometry errors, or a result of systematic effects such as the template choices. Whatever the cause, whilst still producing good agreement with between the best-fit  $z_{\text{phot}}$  and corresponding  $z_{\text{spec}}$  it can result in significantly over or underestimated 1 and 2  $\sigma$  errors. While this systematic effect may be negated when measuring the bulk properties of larger galaxies samples, the method outlined in this paper relies on the direct comparison of individual redshift PDFs so it is essential that they accurately represent the true uncertainties.

We therefore endeavour to ensure the accuracy of our redshift PDFs before undertaking any analysis based on their PDFs. Following the method outlined in Dahlen et al. (2013), we first calculate the fraction of spectroscopic redshifts which fall inside the corresponding 68.3% photo-z con-

Plot to go here...init...

**Figure 1.** Comparison between spectroscopic and photometric redshift for the galaxies in our sample with available spectroscopy and spectroscopic redshift quality of ‘Good’ or better. The photometric redshift shown is the peak of the probability distribution ( $\chi^2$  minimum) with 1- $\sigma$  lower and upper limits.

fidence intervals. Based on the raw PDFs output by EAZY, we find that of XX galaxies with high-quality spectroscopic redshifts at  $z > 2$ , only YY % fall inside the corresponding 1 $\sigma$  PDF confidence intervals, indicating that the our PDF errors are being underestimated. We therefore smooth the PDFs using a boxcar filter and recalculate the fraction of spectroscopic redshift within the 1 $\sigma$ , repeating until this value reaches 68.3%.

Discuss plot

### 3.4 Stellar mass estimation

The stellar mass as a function of redshift,  $M_*(z)$ , for each galaxy is estimated using a modified version of the SED code introduced in Duncan et al. (2014) to which we refer the reader for further details. Rather than estimating the best-fit mass (or mass likelihood distribution) for a fixed input photometric or spectroscopic redshift, we instead estimate the stellar mass at all redshifts in the photometric redshift fitting range simultaneously. Specifically, we calculate the likelihood-weighted mean:

$$M_*(z) = \frac{\sum_t w_t(z) M_{*,t}(z)}{\sum_t w_t(z)} \quad (10)$$

where the sum is over all galaxy template types,  $t$ , with ages less than the age of the Universe at the redshift  $z$  and  $M_{*,t}(z)$  is the optimum stellar mass for each galaxy template (Equation 13). The likelihood,  $w_t(z)$ , is determined by

$$w_t(z) = \exp(-\chi_t^2(z)/2), \quad (11)$$

where  $\chi_t^2(z)$  is given by:

$$\chi_t^2(z) = \sum_j^{N_{\text{filters}}} \frac{(M_{*,t}(z) F_{j,t}(z) - F_j^{\text{obs}})^2}{\sigma_j^2}. \quad (12)$$

The sum is over  $j$  filters available for each galaxy its observed photometric fluxes,  $F_j^{\text{obs}}$  and corresponding error,  $\sigma_j$ . The



optimum scaling for each galaxy template type (each normalised to  $1 M_{\odot}$ ),  $M_{*,t}$ , is calculated analytically by setting the differential of Equation 12 equal to 0 and rearranging to give:

$$M_{*,t}(z) = \frac{\sum_j \frac{F_{j,t}(z)F_j^{obs}}{\sigma_j^2}}{\sum_j \frac{F_{j,t}(z)^2}{\sigma_j^2}}. \quad (13)$$

In this work we also incorporate a so-called “template error function” to account for uncertainties caused by the limited template set and any potential systematic offsets as a function of wavelength. The template error function and method applied to our stellar mass fits is identical to that outlined in [Brammer et al. \(2008\)](#) and included in the initial photometric redshift analysis outlined in Section 3.3. Specifically, this means that the total error for any individual filter,  $j$ , is given by:

$$\sigma_j = \sqrt{\sigma_{j,obs}^2 + (F_{j,obs}\sigma_{temp}(\lambda_j))^2} \quad (14)$$

where  $\sigma_{j,obs}$  is observed photometric flux error,  $F_{j,obs}$  its corresponding flux and  $\sigma_{temp}(\lambda_j)$  the template error function interpolated at the pivot wavelength for that filter,  $\lambda_j$ . We note that in addition to estimating the stellar mass, this method also provides a secondary measurement of the photometric redshift, whereby  $p(z) \propto \sum_t w_t(z)$ . Our decision to use independently estimated redshift PDF in the pair PDF analysis for consistency with [Duncan et al. \(2014\)](#) and the fact that the accuracy offered by EAZY is greater due to its ability to fit non-negative combinations of multiple templates simultaneously ([Brammer et al. 2008](#); [Dahlen et al. 2013](#)).

For the [Bruzual & Charlot \(2003\)](#) templates used in our stellar mass fitting we allow a similar range of stellar population parameters as used in [Duncan et al. \(2014\)](#). Model ages are allowed to vary from 10 Myr to the age of the Universe at a given redshift, metallicities of 0.02, 0.2 and  $1 Z_{\odot}$ , and dust attenuation strength in the range  $0 \leq A_V \leq 3$  assuming a [Calzetti et al. \(2000\)](#) attenuation curve. The assumed star-formation histories follow exponential  $\tau$ -models ( $SFR \propto e^{-t/\tau}$ ), both decreasing and increasing (negative  $\tau$ ), for characteristic timescales of  $|\tau| = 0.25, 0.5, 1, 2.5, 5, 10$ , plus an additional short burst ( $\tau = 0.05$ ) and continuous star-formation models ( $\tau \gg 1/H_0$ ).

Nebular emission is included assuming a relatively high escape fraction  $f_{esc} = 0.2$  ([Yajima et al. 2010](#); [Fernandez & Shull 2011](#); [Finkelstein et al. 2012](#); [Robertson et al. 2013](#)) and hence a relatively conservative estimate on the contribution of nebular emission. As in [Duncan et al. \(2014\)](#), we assume for the nebular emission that the gas-phase stellar metallicities are equivalent and that stellar and nebular emission are attenuated by dust equally.

### 3.5 Correction for selection effects

As defined by [López-Sanjuan et al. \(2015\)](#), the pair-probability function in Equation 9 is affected by two selection effects. Firstly, the incompleteness in search area around

galaxies which are near the image boundaries or near areas affected by bright stars (Section 3.5.2). And secondly, the selection in photometric redshift quality (Section 3.5.3). Additionally, because in this work we use a flux-limited sample rather than a volume-limited as used by [López-Sanjuan et al. \(2015\)](#), we must also include a further correction to account for this.

#### 3.5.1 The redshift dependent mass-limit

Since the photometric survey we are using includes regions of different depth and high-redshift galaxies are by their very nature quite faint, restricting our analysis to a volume limited sample would necessitate excluding the vast majority of the available data. As such, we choose to use a redshift dependent mass completeness limit with the limit determined by the flux limit determined by the survey.

Due to the limited number of galaxy sources available, determining the strict mass completeness as a function of redshift entirely empirically ([Pozzetti et al. 2010](#)) is not possible. Instead, we make use of a semi-empirical method based on that of [Pozzetti et al. \(2010\)](#), using the available observed stellar mass estimates to inform the selection of a template SED for the evolving 95% stellar mass-to-light limit. We make use of the full set of high-redshift Monte Carlo samples of [Duncan et al. \(2014\)](#), selecting galaxies which are within a given redshift bin, then scaling the masses of the faintest 20% such that their apparent magnitude is equal to the flux limit. The mass completeness limit for a given redshift bin is defined as the mass corresponding to the 95th percentile of the scaled mass range, the resulting mass completeness at  $z > 3.5$  in bins with width  $\Delta z = 0.5$  are shown in Figure 3 assuming a flux-limit equal to that in the GOODS South ‘DEEP’ region.

Based on the estimated completeness limits, we select a [Bruzual & Charlot \(2003\)](#) template which closely matches the observed  $M_{*}/L$  redshift evolution. By doing so we can estimate the mass completeness as a continuous function of redshift and extend the constraints to redshifts lower than those explored in [Duncan et al. \(2014\)](#). A common choice of template for estimating the strict  $M_{*}/L$  completeness is a maximally old single burst (continuous blue line in Figure 3). However, since the vast majority of galaxies above  $z \sim 3$  are star-forming this assumption significantly overestimates the actual completeness limit at high-redshift. Based on plausible assumptions for galaxies at high-redshift and tuning by hand, we find a maximally old, dusty ( $A_V = 2$ ) star-forming galaxy with a power-law star-formation history ( $\propto t^{1.4}$ ) provides a good fit to the empirical data (red dashed line in Figure 3). For both the burst and star-forming SEDs, we assume an onset of star-formation at  $z = 12$ , sub-solar metallicity ( $0.2 Z_{\odot}$ ) and an escape fraction for nebular emission of  $f_{esc} = 0.2$ .

The redshift dependent mass limit,  $M_{*}^{\text{flux}}(z)$ , is defined as

$$\log_{10}(M_{*}^{\text{flux}}(z)) = 0.4 \times (H_{M_{*}/L}(z) - H^{\text{lim}}) \quad (15)$$

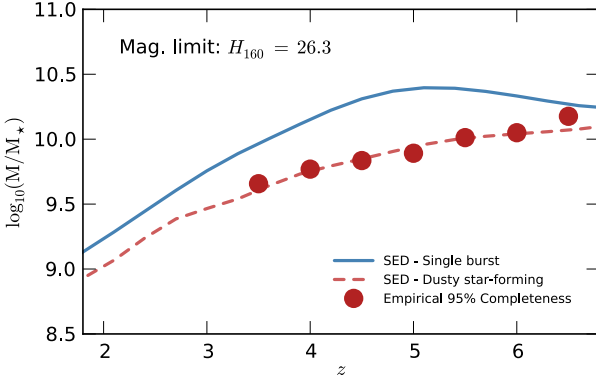


**Figure 2.** Mass completeness limit corresponding to a flux limit of  $H_{160} = 26.3$ , the approximate depth of the DEEP and ERS regions within CANDELS GOODS South. Red circles correspond to the 95% completeness limits derived from Duncan et al. (2014) the continuous blue and dashed red lines are the completeness limits corresponding to a maximally old (at a given redshift) single burst or dusty star-forming population respectively, see text for details.

where  $H^{\text{lim}}$  is the  $H_{160}$  magnitude at the flux-completeness limit in the field or region of interest and  $H_{M_*/L}(z)$  is the  $H_{160}$  magnitude of the dusty star-forming template normalised to  $1 M_\odot$  and observed through the  $H_{160}$  at a given redshift (automatically taking the required  $k$ -correction into account).

For a primary galaxy with a mass close to the redshift dependent mass-limit imposed by the selection criteria  $S(z)$ , the mass range within which secondary pairs can included may be reduced, i.e.  $\mu M_*^1(z) < M_*^{\text{lim}}(z) < M_*^1(z)$ . To correct for the potential galaxy pairs which may be lost by the applied completeness limit, we make a statistical correction based on the stellar mass function at the redshift of interest. The flux-limit weight is defined as

$$w_{\text{flux}}^2(z) = \frac{1}{W_2(z)}, \quad (16)$$

where

$$W_2(z) = \frac{\int_{M_*^{\text{lim}}(z)}^{M_*^1(z)} \phi(M_*|z) dM_*}{\int_{\mu M_*^1(z)}^{M_*^1(z)} \phi(M_*|z) dM_*} \quad (17)$$

and  $\phi(M_*|z)$  is the stellar mass function at the corresponding redshift. The redshift dependent mass limit is  $M_*^{\text{lim}}(z) = \max\{\mu M_*^1(z), M_*^{\text{flux}}(z)\}$ , where  $M_*^{\text{flux}}(z)$  is defined in Equation 15). By applying this weight to all pairs associated with a primary galaxy, we get the the pair statistics corresponding to  $\mu M_*^1(z) \leq M_*^2(z) \leq M_*^1(z)$  (the volume limited case). As in Patton et al. (2000), we assign additional weights to the primary sample in order to minimise the error from primary galaxies which are closer to the flux limit (i.e. PDF weighted to higher redshifts) as these galaxies will have fewer numbers of *observed* pairs. The primary flux-weight,  $w_{\text{flux}}^1(z)$  is

defined as

$$w_{\text{flux}}^1(z) = W_1(z) = \frac{\int_{M_*^{\text{lim}}(z)}^{M_*^{\text{max}}} \phi(M_*|z) dM_*}{\int_{M_*^{\text{min}}}^{M_*^{\text{max}}} \phi(M_*|z) dM_*} \quad (18)$$

where  $M_*^{\text{min}}$  and  $M_*^{\text{max}}$  are the lower and upper limits of the mass range of interest for the primary galaxy sample, the redshift dependent lower limit is defined as  $M_*^{\text{lim}}(z) = \max\{M_*^{\text{min}}, M_*^{\text{flux}}(z)\}$ , and the remaining parameters are as outlined above. In the case of a volume limited sample (where  $M_*^{\text{flux}}(z) < \mu M_*^1(z)$  at all redshifts) both of the flux-limit weights are equal to unity.

The stellar mass functions (SMF) parametrisations as a function of redshift,  $\phi(M_*|z)$ , are taken from (Mortlock et al. 2014) at  $z \leq 3$ , (Santini et al. 2012) at  $3 < z < 3.5$  and Duncan et al. (2014) at  $z \geq 3.5$ . When selecting redshift bins in which to estimate the merger fraction, we ensure that the bins are chosen to match the bins in which the SMF are constrained (i.e. the SMF used to weight the merger fraction is the same across the bin).

### 3.5.2 Image boundary and excluded regions

A second correction which must be taken into account is to the search area around primary galaxies which lie close to the boundaries of the survey region. Because of the fixed physical search distance, this correction is also a function of redshift so must be calculated for all redshifts within the range of interest.

In addition to the area lost at the survey boundaries, it is also necessary to correct for the potential search area lost due to the presence of large stars and other artefacts (around which no source are included in the catalog, see Section (ref sample cleaning)).

We have taken both of these effects into account when correcting for the search areas by creating a mask image based on the underlying photometry. Firstly, we define the image boundary based on the exposure map corresponding to the  $H_{160}$  photometry used for object detection. Next, for every source excluded from the sample catalog based its classification as a star or image artefact by our photometric or visual classification, the area corresponding that object (from the photometry segmentation map) is set to zero in our mask image. Finally, areas of photometry which are labelled in the flag map (and excluded based on their corresponding catalog flags) are also set to zero.

To calculate the area around a primary galaxy which is excluded by these effects, we perform photometry on the mask image. Photometry is performed in annuli around each primary galaxy target, with inner and outer radii of  $\theta_{\text{min}}(z)$  and  $\theta_{\text{max}}(z)$  respectively. The area weight is then defined as

$$w_{\text{area}}(z) = \frac{1}{f_{\text{area}}(z)} \quad (19)$$

where  $f_{\text{area}}(z)$  is the sum of the normalised mask image within the annulus at a given redshift divided by the sum over the same area in an image with all values equal to unity.

By measuring the area in this way we are able to automatically take into account the irregular survey shape and any small calculation errors from quantisation of areas due to finite pixel size.

### 3.5.3 The Odds sampling rate

Following López-Sanjuan et al. (2015), we also apply a selection based on the photometric redshift quality, or odds  $\mathcal{O}$  parameter. The odds parameter is defined by Benítez (2000) and Molino et al. (2014) as

$$\mathcal{O} = \int_{-K(1+z_p)}^{+K(1+z_p)} P(z) dz \quad (20)$$

where  $z_p$  is the redshift corresponding peak of the redshift PDF,  $P(z)$  (or the PDF average or median). In Molino et al. (2014)  $K = 0.0125$ , however due to the high redshifts of interest and the broadband nature of the CANDELS survey (as opposed to the lower redshift narrow-band ALHAMBRA survey studied in Molino et al. (2014)) we assume a broader criteria of  $K = 0.05$  (*CHECK AND/OR JUSTIFY*). The odds sampling rate (OSR) for galaxies with an apparent  $H_{160}$  magnitude of  $M$  is then defined as

$$\text{OSR}(M) = \frac{\sum_i N_{i, \mathcal{O} \geq 0.3}}{\sum_i N_{i, \mathcal{O} \geq 0}}, \quad (21)$$

the ratio between the number of galaxies with  $\mathcal{O} \geq 0.3$  and the total number of galaxies ( $\mathcal{O} \geq 0$ ) with magnitude  $M$ .

We first calculate  $\text{OSR}(M)$  in bins with width  $\Delta M = 0.5$  and interpolate these values to define the odds sampling rate for each galaxy based on its apparent  $H_{160}$  magnitude. From this value, the OSR weight for each individual galaxy,  $i$ , is then defined as

$$w_{\text{OSR}}^i = \frac{1}{\text{OSR}(M_i)}. \quad (22)$$

### 3.5.4 The combined weights

Taking all three of the above effects into account, the pair weights for each secondary galaxy found around a galaxy primary are given by

$$w_2(z) = w_{\text{area}}^1(z) \times w_{\text{flux}}^1(z) \times w_{\text{flux}}^2(z) \times w_{\text{OSR}}^1 \times w_{\text{OSR}}^2. \quad (23)$$

The weights applied to every primary galaxy in the sample are then given by

$$w_1 = w_{\text{flux}}^1(z) \times w_{\text{OSR}}^1. \quad (24)$$

These weights are then applied to the integrated pair-probability functions for each set of potential pairs to calculate the merger fraction.

## 3.6 The merger fraction

For each galaxy,  $i$ , in the primary sample, the number of associated pairs,  $N_{\text{pair}}^i$ , within the redshift range  $z_{\min} < z <$

$z_{\max}$  is given by

$$N_{\text{pair}}^i = \sum_j \int_{z_{\min}}^{z_{\max}} w_2^j(z) \times \text{PPF}_j(z) dz \quad (25)$$

where  $j$  indexes the number of potential close pairs found around the primary galaxy,  $\text{PPF}_j(z)$  the corresponding pair-probability function (Section 3.2) and  $w_2^j(z)$  its pair weight (Equation 23). The corresponding weighted primary galaxy contribution,  $N_1^i$ , within the redshift bin is

$$N_1^i = \sum_i \int_{z_{\min}}^{z_{\max}} w_1^i(z) \times P_i(z) \times S_1^i(z) dz \quad (26)$$

where  $S_1^i(z)$  is the selection function for the primary galaxies given in Equation 8,  $P_i(z)$  its normalised redshift probability distribution and  $w_1^i$  its weighting. In the case of a primary galaxy with stellar mass in the desired range with its redshift PDF contained entirely within the redshift range of interest,  $N_1^i = w_1^i$  and hence always equal or greater than unity.

The estimated merger fraction  $f_m$  in the redshift range  $z_{\min} < z < z_{\max}$  is then given by

$$f_m = \frac{\sum_i N_{\text{pair}}^i}{\sum_i N_1^i} \quad (27)$$

where  $i$  is summed over all galaxies in the primary sample. In the case of a field which consists of different sub-fields with differing depths like GOODS South. This sum becomes

$$f_m = \frac{\sum_k \sum_i N_{\text{pair}}^{k,i}}{\sum_k \sum_i N_1^{k,i}} \quad (28)$$

where  $k$  is indexed over the number distinct regions within a field (in the case of GOODS South – Deep, Wide, ERS and UDF) and the flux-limited mass completeness used throughout the calculations is set by the corresponding  $H_{160}$  depth within each field.

## 4 THE MERGER EVOLUTION AT $Z > 2$

For this work we select our initial sample of galaxies in each field based on the following criteria:

$$\int_2^\infty P(z) dz > 0.95, \quad (29)$$

ensuring that the bulk of the redshift probability distribution lies at high redshift and that any secondary redshift solutions are minor.

### 4.1 Merger fractions for semi-analytic models

To make a direct comparison with theoretical models and negate any uncertainty due to assumed merger timescales when comparing merger rates, we also perform the pair-count analysis on mock lightcones from the semi-analytic models of Lu et al. (2011, see also Lu et al. 2014). We treat the mock data as a ‘perfect’ spectroscopic survey and apply a pseudo-spectroscopic pair-count methodology for the same

separation and mass criteria as used on the observational data, using a separation criteria of  $\Delta v \leq 500 \text{ km s}^{-1}$  along the line-of-sight.

Although the field size of the lightcone is approximately  $10\times$  the size of the observed GOODS South field, the counts obtained are still subject to significant errors due to cosmic variance. To minimise the effects of cosmic variance, we apply the analysis to 8 different realisations of the mock lightcone, taking the average and standard deviation of these values. We calculate the pair-counts for overlapping redshift bins with width  $\Delta z = 0.5$ , in steps of half this size. Due to volume limitations at low-redshift and the simulation time and resolution limits at high-redshift, we restrict the mock pair-count analysis to  $0.5 \leq z \leq 5.75$ .

## 4.2 Evolution of the pair fraction



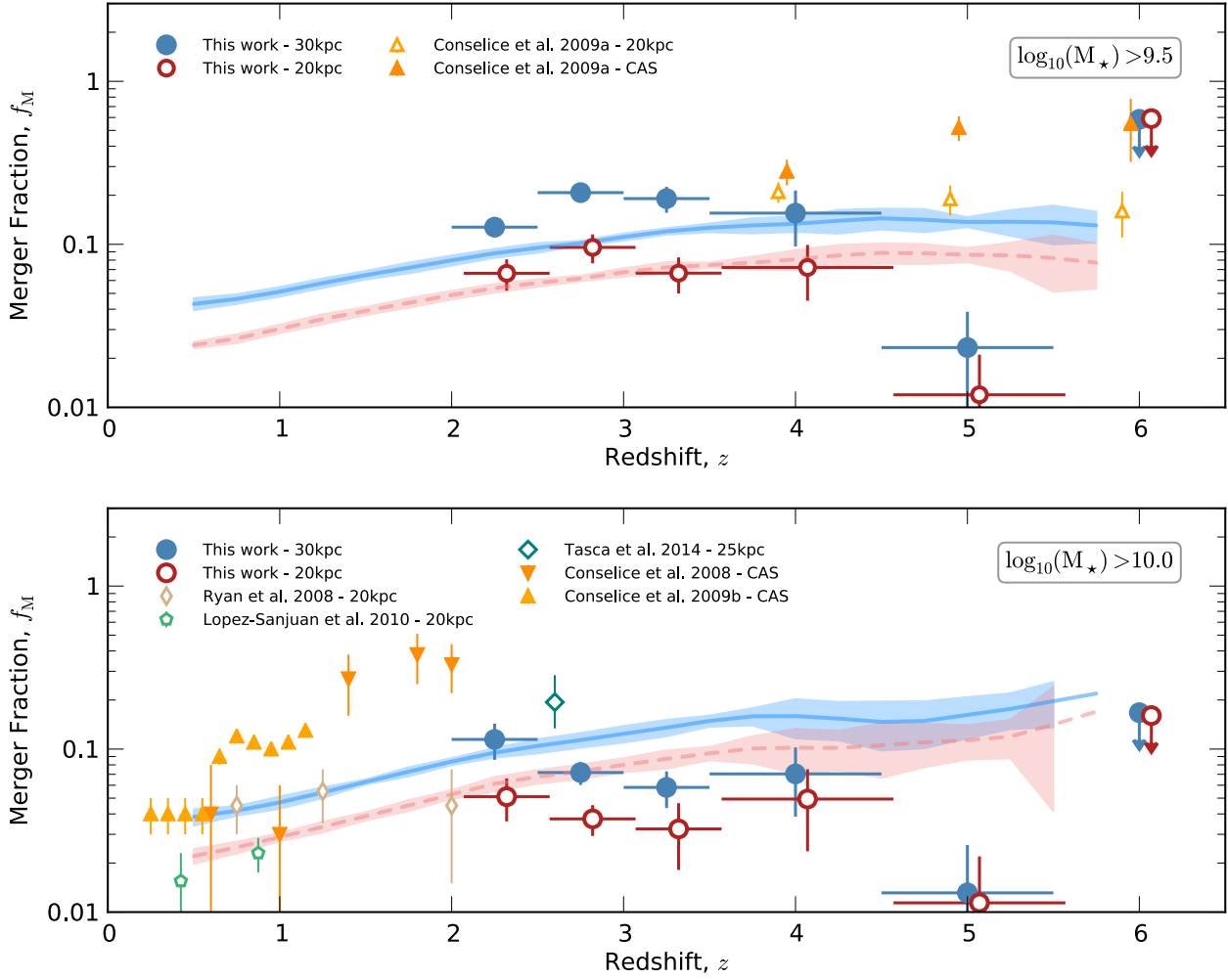


Figure 3.

## ACKNOWLEDGEMENTS

Thanks.



## REFERENCES

- Beckwith S. V. W., et al., 2006, *The Astronomical Journal*, 132, 1729
- Behroozi P. S., Wechsler R. H., Conroy C., 2013, *ApJ*, 770, 57
- Bell E. F., Phleps S., Somerville R. S., Wolf C., Borch A., Meisenheimer K., 2006, *ApJ*, 652, 270
- Benítez N., 2000, *ApJ*, 536, 571
- Bluck A. F. L., Conselice C. J., Bouwens R. J., Daddi E., Dickinson M., Papovich C., Yan H., 2009, *MNRAS: Letters*, 394, L51
- Bluck A. F. L., Conselice C. J., Buitrago F., Grützbauch R., Hoyos C., Mortlock A., Bauer A. E., 2012, *ApJ*, 747, 34
- Bouwens R. J., et al., 2014, eprint arXiv:1403.4295
- Brammer G. B., van Dokkum P. G., Coppi P., 2008, *ApJ*, 686, 1503
- Bruzual G., Charlot S., 2003, *MNRAS*, 344, 1000
- Bundy K., Fukugita M., Ellis R. S., Targett T. A., Belli S., Kodama T., 2009, *ApJ*, 697, 1369
- Calzetti D., Armus L., Bohlin R. C., Kinney A. L., Koornneef J., Storchi-Bergmann T., 2000, *ApJ*, 533, 682
- Conselice C. J., Arnold J., 2009, *MNRAS*, 397, 208
- Conselice C. J., Bershadsky M. A., Dickinson M., Papovich C., 2003, *The Astronomical Journal*, 126, 1183
- Conselice C. J., Rajgor S., Myers R., 2008, *MNRAS*, 386, 909
- Dahlen T., et al., 2013, *ApJ*, 775, 93
- Duncan K., et al., 2014, *MNRAS*, 444, 2960
- Erb D. K., Pettini M., Shapley A. E., Steidel C. C., Law D. R., Reddy N. A., 2010, *ApJ*, 719, 1168
- Fernandez E., Shull J. M., 2011, *ApJ*, 731, 20
- Finkelstein S. L., et al., 2012, *ApJ*, 758, 93
- Grogin N. A., et al., 2011, *ApJS*, 197, 35
- Guo Y., et al., 2013, *ApJS*, 207, 24
- Henriques B. M. B., White S. D. M., Lemson G., Thomas P. A., Guo Q., Marleau G.-D., Overzier R. A., 2012, *MNRAS*, 421, 2904
- Hildebrandt H., Wolf C., Benitez N., 2008, *A&A*, 480, 703
- Hopkins A. M., Beacom J. F., 2006, *ApJ*, 651, 142
- Hopkins P. F., et al., 2010, *ApJ*, 724, 915
- Kartaltepe J. S., et al., 2007, *ApJS*, 172, 320
- Kennicutt Jr R. C., 1998, *ApJ*, 498, 541
- Kitzbichler M. G., White S. D. M., 2008, *MNRAS*, 391, 1489
- Koekemoer A. M., et al., 2011, *ApJS*, 197, 36
- Le Fèvre O., et al., 2000, *MNRAS*, 311, 565
- López-Sanjuan C., Balcells M., Pérez-González P. G., Barro G., Gallego J., Zamorano J., 2010, *A&A*, 518, A20
- López-Sanjuan C., et al., 2015, *A&A*, 576, A53
- Lotz J. M., Jonsson P., Cox T. J., Primack J. R., 2010a, *MNRAS*, 404, 575
- Lotz J. M., Jonsson P., Cox T. J., Primack J. R., 2010b, *MNRAS*, 404, 590
- Lu Y., Mo H. J., Weinberg M. D., Katz N., 2011, *MNRAS*, 416, 1949
- Lu Y., et al., 2014, *ApJ*, 795, 123
- Maneewongvatana S., Mount D. M., 1999, eprint arXiv:cs/9901013
- McLure R. J., et al., 2011, *MNRAS*, 418, 2074
- Molino A., et al., 2014, *MNRAS*, 441, 2891
- Mortlock A., et al., 2014, *MNRAS*, 447, 2
- Oke J. B., Gunn J. E., 1983, *ApJ*, 266, 713
- Ownsworth J. R., Conselice C. J., Mortlock A., Hartley W. G., Almaini O., Duncan K., Mundy C. J., 2014, *MNRAS*, 445, 2198
- Patton D. R., Carlberg R. G., Marzke R. O., Pritchett C. J., da Costa L. N., Pellegrini P. S., 2000, *ApJ*, 536, 153
- Pozzetti L., et al., 2010, *A&A*, 523, A13
- Robertson B. E., et al., 2013, *ApJ*, 768, 71
- Ryan Jr R. E., Cohen S. H., Windhorst R. A., Silk J., 2008, *ApJ*, 678, 751
- Santini P., et al., 2012, *A&A*, 538, A33
- Stark D. P., et al., 2014, eprint arXiv:1408.3649
- Yajima H., Choi J.-H., Nagamine K., 2010, *MNRAS*, 412, 411